

An Architecture Study for Low-Power Satellite-Based Wildlife Tracking

Fausto Vega
The Robotics Institute
Carnegie Mellon University
Pittsburgh, PA 15213
fvega@andrew.cmu.edu

Robert MacCurdy
Mechanical Engineering
University of Colorado
Boulder, CO 80309
maccurdy@colorado.edu

James Phillips
Computer Science
University of Colorado
Boulder, CO 80309
James.Phillips-1@colorado.edu

Zachary Manchester
The Robotics Institute
Carnegie Mellon University
Pittsburgh, PA 15213
zacm@cmu.edu

Kathryn Lampo
Mechanical Engineering
Columbia University
New York, NY 10027
k.lampo@columbia.edu

Abstract—Accurate satellite-based positioning has revolutionized several industries over the past two decades, from agriculture to transportation. However, conventional GNSS receivers consume significant energy and are too large for many wildlife-tracking applications, which are of critical importance to conservation efforts and our understanding of the global climate. To address this capability gap, we propose a new positioning system designed from the outset to minimize the size, mass, power, and cost of the terrestrial tracking device. We analyze, through extensive modeling and simulation, a mission concept that relies on space-based receivers hosted on a constellation of small satellites in low-Earth orbit that detect and localize signals from very small transmitter tags. We compare a variety of signal modulations, frequencies, and positioning techniques, including both Doppler and time-of-arrival methods, and evaluate the transmitter power required, minimum number of satellites, and achievable position accuracy across a range of design parameters. Our model accounts for errors in satellite orbital state knowledge, clock offsets, frequency measurement errors, and ionospheric effects. This paper presents the results of our extensive trade study, as well as hardware field experiments performed outdoors using flight-traceable software-defined radio receivers.



Figure 1. Field testing results overlaid on a satellite photo of the test site. The yellow line shows ground-truth GPS measurements while the red dots are positions calculated with our time-of-arrival system. The RMS difference between our system and GPS is approximately 22.6 meters.

TABLE OF CONTENTS

1. INTRODUCTION.....	1
2. BACKGROUND	2
3. CANDIDATE SYSTEM ARCHITECTURES.....	3
4. NAVIGATION ALGORITHMS	3
5. SOFTWARE-MODELING TOOL	5
6. RESULTS	5
7. EXPERIMENTAL VALIDATION	6
8. CONCLUSIONS.....	9
ACKNOWLEDGMENTS	10
REFERENCES	10
APPENDICES.....	11
A. IMPLICIT FUNCTION THEOREM.....	11
B. DOPPLER DERIVATIONS	11
C. ADDITIONAL PLOTS	11
BIOGRAPHY	15

1. INTRODUCTION

Satellite-based positioning emerged in the 1960s with the development of TRANSIT, a satellite-navigation system that utilized the Doppler shift induced by relative motion between satellites and terrestrial receivers to provide infrequent position updates for Polaris ballistic missile submarines [1]. The need for continuous positioning led to the development of the global positioning system (GPS), which currently consists of a thirty-one-satellite constellation in medium-Earth orbit using time-of-arrival measurements to provide positioning information [2]. GPS has impacted a wide range of domains, from agriculture to transportation, by providing high-accuracy positioning information. However, the size, weight, energy consumption, and cost of GPS receivers limits their use in many applications, including wildlife tracking, which is essential for our understanding of the global climate, as species migration is an important indicator of climate change [3]. Conservation efforts for endangered species also benefit from accurate wildlife position data [4] [5].

Another approach to wildlife tracking, ARGOS, relies on Doppler-based positioning like TRANSIT [6]. While ARGOS reports achievable position accuracies in the range of 150 m - 2500 m, field testing on sea turtles [7] and bottlenose

dolphins [8] equipped with both GPS and ARGOS tags have demonstrated that errors are most commonly in the kilometer range. The cost of ARGOS transmitting tags range from \$1500-\$4000, which limits for large-scale deployments [6], and the smallest ARGOS tags weigh around 5 grams [9], however they deliver very few position fixes. The Icarus Initiative is another small-animal tracking system that uses a receiver hosted on the International Space Station (ISS) to gather position data recorded by GPS receivers onboard ICARUS tags, in addition to temperature, pressure, and accelerometer data, to observe animal behavior and monitor the environment [10].

To address the cost, accuracy, and size limitations of existing methods, we propose a new approach to wildlife tracking that relies on space-based receivers hosted on a constellation of small satellites in low-Earth orbit that detect and localize signals from very small transmitting tags. The transmitting tags are lightweight, low-cost, and consume minimal energy [11]. In this work, we analyze, through extensive modeling and simulation, the positioning accuracy that can be achieved by a small-satellite constellation receiving signals from very small, light-weight transmitting tags placed on animals. Our contributions include:

- A Kalman filtering approach to estimate the position and velocity of a low-Earth orbit (LEO) satellite to very high accuracy from GPS measurements.
- A unified algorithmic approach for tag localization using a combination of Doppler and time-of-arrival (TOA) measurements.
- Full end-to-end system modeling and a constellation-design trade study.
- Hardware validation of flight-traceable receivers and tags in outdoor field tests.

The paper proceeds as follows: We introduce measurement, dynamics, and error models in Section 2. Next, we describe candidate system architectures in Section 3, and present a detailed description of the navigation algorithms used for the simulations in Section 4. A software modeling tool to aid in constellation geometry design is then detailed in Section 5, followed by trade-study outcomes in Section 6. Section 7 presents the results of outdoor hardware validation tests. Finally, Section 8 summarizes our conclusions and directions for future work.

2. BACKGROUND

This section describes the measurement models used for tracking, along with the satellite dynamics model utilized in the extended Kalman filter to determine the satellite's orbital state.

TOA Measurement Model

Time-of-arrival systems measure the transit time of the signal from the transmitting tag to the receiver onboard the satellite. The satellite and transmitter clocks are not synchronized; therefore, the measurement is biased. The TOA measurement model is described by,

$$\rho = ct_m = \|\vec{r}_{tag} - A\vec{r}_{sat}\| + c\tau + I_\rho + \eta, \quad (1)$$

$$A = \begin{bmatrix} \cos\omega_E t_m & \sin\omega_E t_m & 0 \\ -\sin\omega_E t_m & \cos\omega_E t_m & 0 \\ 0 & 0 & 1 \end{bmatrix}, \quad (2)$$

where ρ is known as a “pseudorange,” t_m represents the transit time, \vec{r}_{tag} is the position of the transmitting tag in the Earth-centered-Earth-fixed (ECEF) frame, \vec{r}_{sat} is the position of the satellite in the Earth-centered-inertial (ECI) frame, τ represents the clock bias, I_ρ is the delay caused by the ionosphere, η represents random noise due to sensor uncertainty, c is the speed of light in a vacuum, and A is a rotation matrix to transform the position of the satellites (\vec{r}_{sat}) from the ECI frame to the ECEF frame at the receiving time. This transformation considers the magnitude of the Earth's rate of rotation (ω_E), along with the transit time of the signal. This rotation of the Earth during signal transit is small, but can introduce an error of 10-20 m in the range computation, which induces an east-west error in the position estimate [2]. Using this model, we estimate the position of the tag (\vec{r}_{tag}) in Cartesian coordinates in the ECEF frame as well as the clock bias (τ).

Doppler Measurement Model

The Doppler measurement model records the change between the transmitted and received frequencies (Δf) that occurs due to the relative motion of the spacecraft with respect to the tag (Doppler shift). This measurement depends on the time derivative of (1) and the transmitted frequency (f_0).

$$\Delta f = f_0 \frac{\frac{\partial}{\partial t}(\|\vec{r}_{tag} - A\vec{r}_{sat}\|)}{c} + \dot{b} + \dot{I}_\rho + \eta \quad (3)$$

Similar to (1), we estimate the position of the tag (\vec{r}_{tag}) in Cartesian coordinates as well as a frequency offset term (\dot{b}). A derivation of the time derivative of the true range is provided in the Appendix.

Ionospheric Effects

The ionosphere is a region of the atmosphere extending from about 50 to 1000 km altitude that is ionized by radiation from the sun. The physical characteristics of the ionosphere vary over a large range and are unpredictable [2]. The ionosphere can be modeled as a thin shell at a height h_I above the Earth, producing a delay in the pseudorange measurement modeled by,

$$I_\rho = \frac{40.3 TECV}{f^2} \left[1 - \left(\frac{R_E \sin(\zeta)}{R_E + h_I} \right)^2 \right]^{\frac{-1}{2}}, \quad (4)$$

where ζ is the zenith angle of the satellite, R_E is the radius of the Earth, f is the frequency of the signal, and $TECV$ is the total electron count (TEC) value in the zenith direction [2]. The effect of the ionosphere on Doppler measurements is the time derivative of the delay in (4):

$$\dot{I}_\rho = \frac{(40.3 TECV) \left(\frac{(R_E \sin(\zeta))(R_E \cos(\zeta)\dot{\zeta})}{(R_E + h_I)^2} \right)}{f^2 \left(1 - \left(\frac{R_E \sin(\zeta)}{R_E + h_I} \right)^2 \right)^{\frac{3}{2}}}. \quad (5)$$

Satellite Dynamics

We perform ground-truth simulations of the satellite's orbital dynamics using the open-source Julia package *SatelliteDynamics.jl*, which includes high-order gravity models, n-body

effects due to the sun and moon, atmospheric drag force, and solar radiation pressure [12]. However, computing the Jacobian of this high-fidelity dynamics model is expensive and unnecessary onboard a satellite. Therefore, we use a simplified dynamics model that only considers the gravitational force up to J2 and the drag force as the process model in the estimation algorithms that follow. The acceleration due to gravity is given by:

$$\vec{a}_{J2} = \frac{-\mu \vec{r}_{sat}}{\|\vec{r}_{sat}\|^3} + \frac{3\mu J_2 R_E^2}{2\|\vec{r}_{sat}\|^5} \left(\frac{5(\vec{r}_{sat} \cdot \vec{I}_z)^2}{\|\vec{r}_{sat}\|^2} - 1 \right) \vec{r}_{sat} - 2(\vec{r}_{sat} \cdot \vec{I}_z)\vec{I}_z \quad (6)$$

where R_E is the radius of the Earth, J_2 is the harmonic coefficient due to the oblateness of the Earth, μ is the gravitational parameter, and \vec{I}_z corresponds to the unit vector pointing in the z direction [13].

Similarly, the drag force is modeled by,

$$\vec{a}_d = -\frac{1}{2}\rho_a A_c c_d \|\vec{v}_r\| \vec{v}_r, \quad (7)$$

where,

$$\vec{v}_r = \vec{v}_{sat} - \vec{\omega}_E \times \vec{r}_{sat} \quad (8)$$

where A_c represents the cross-sectional area in the direction of incoming flow, ρ_a is the atmospheric density, c_d is the drag coefficient, and v_r is the spacecraft velocity relative to the atmosphere expressed in (8). The relative velocity \vec{v}_r is dependent on the angular rate of rotation of the Earth ($\vec{\omega}_E$) along with the satellite velocity (\vec{v}_{sat}) and satellite position (\vec{r}_{sat}) in Cartesian coordinates. We assume a constant cross-sectional area (A_c).

3. CANDIDATE SYSTEM ARCHITECTURES

We evaluate several candidate system architectures: four satellites performing TOA measurements, four satellites performing Doppler measurements, and seven satellites performing Doppler measurements. Each architecture requires the satellites to fly in formation, as depicted in Fig. 2. We also analyze single- and dual-frequency versions of each of these architectures.

Time-of-Arrival Formations

The TOA method requires precision timing from multiple receivers with synchronized clocks. We assume clock synchronization errors of 20 ns based on hardware tests conducted in [3].

The use of a single frequency for TOA measurements produces biased tag position and clock bias estimates due to ionospheric effects. Using two frequencies enables estimation of the ionosphere TEC value and elimination of this bias, resulting in improved accuracy.

Doppler-Based Formations

The Doppler method does not rely on precise time synchronization between receiver clocks, but requires extremely

precise frequency references [2]. Oscillator frequency instability produces significant tag-position errors. We assume frequency errors around 1 Hz.

Because it depends on the difference in velocity between transmitter and receiver, the Doppler method is also very sensitive to tag motion, and assume a stationary tag. Modest tag motion can induce a large position bias. These effects can be mitigated by introducing more satellites: A four-satellite Doppler system can estimate out the tag position along with a frequency bias term, and a seven-satellite Doppler system can additionally estimate out the velocity of the tag.

Table 1 summarizes the system architectures that are considered, along with a number label to reference these architectures in Section 6.

Table 1. Candidate System Architectures

Label	Configuration
1	4 Satellites TOA 1 frequency
2	4 Satellites TOA 2 frequencies
3	4 Satellites Doppler 1 frequency
4	4 Satellites Doppler 2 frequencies
5	7 Satellites Doppler 1 frequency
6	7 Satellites Doppler 2 frequencies

Section 6 will evaluate the positioning performance for each of the system architectures.

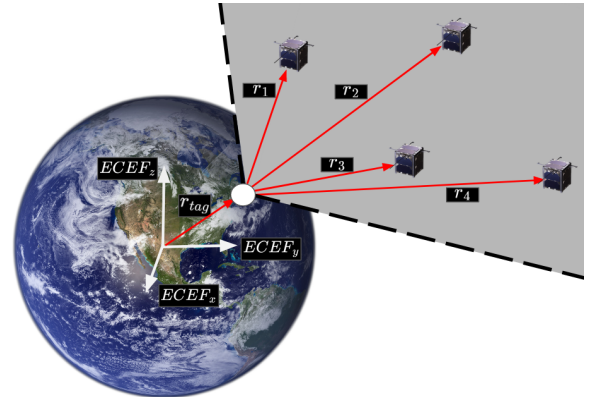


Figure 2. Tag horizon (grey) with the vectors (red) depicting the true range between the satellite and the tag position in the ECEF frame

4. NAVIGATION ALGORITHMS

We address two facets of the navigation problem posed in this paper: Estimating tag positions given precise satellite positions and tag signal measurements, and estimating the satellite positions and velocities with very high accuracy from GPS measurements. We begin with the latter in this section.

Satellite GPS Filter

We determine the state of the satellites using a square-root extended Kalman filter (SREKF). First, a reference orbit is generated using an accurate dynamics model with gravity order 10 and degree 10 using *SatelliteDynamics.jl* [12]. Next,

we generate simulated GPS measurements by adding Gaussian noise with a standard deviation of 10m to the reference orbit positions. The filter's process model consists of satellite dynamics that only consider the gravitational force, J2, and drag described in (12). Since we utilize a simplified dynamics model, we also estimate out the truncated higher-order accelerations because they do not behave like additive white Gaussian noise. We model these accelerations ($\vec{\varepsilon}$) as a first-order Gauss-Markov model expressed by the following:

$$\begin{aligned}\dot{\vec{\varepsilon}} &= -B(t)\vec{\varepsilon} + w(t) \\ w(t) &\sim \mathcal{N}(0, Q_\varepsilon)\end{aligned}\quad (9)$$

where $B(t)$ is a 3×3 time-correlation matrix, which is a diagonal matrix of the time correlation coefficients ($\beta \in \mathbb{R}^3$). These time correlation coefficients are also added to the state and we assume they follow a random walk model:

$$\begin{aligned}\dot{\beta} &= u(t) \\ u(t) &\sim \mathcal{N}(0, Q_\beta)\end{aligned}\quad (10)$$

This method is known as dynamic model compensation (DMC) and it has been shown to provide more accurate state estimates for lunar satellites using Apollo 10 [14] and near-Earth orbiter data [15]. Model errors are always present due to uncertainties in atmospheric density models, variations in solar radiation pressure, and tidal forces, etc [15]. The disadvantage of this method is an increase in the size of the EKF state vector, resulting in increased computational cost [16].

The filter state, denoted as x , includes the satellite position (\vec{r}_{sat}), velocity (\vec{v}_{sat}), as well as the unmodeled accelerations ($\vec{\varepsilon}$), and time correlation parameters (β):

$$x = \begin{bmatrix} \vec{r}_{sat} \\ \vec{v}_{sat} \\ \vec{\varepsilon} \\ \beta \end{bmatrix} \in \mathbb{R}^{12} \quad (11)$$

The continuous nonlinear dynamics model is as follows:

$$\dot{x} = \begin{bmatrix} \vec{v}_{sat} \\ \vec{a}_{gJ2} + \vec{a}_d + \vec{\varepsilon} \\ \dot{\vec{\varepsilon}} \\ \dot{\beta} \end{bmatrix} \quad (12)$$

We assume the measurement model provides the position of the satellite and is represented by the following:

$$h(x) = [I(3) \quad 0_{3 \times 6}] x \quad (13)$$

We use an analytical representation of the process noise covariance derived in [17], and the simulation timestep is set to 1 s. We implement an SREKF using the QR decomposition to handle covariance updates [18]. This variant of the Kalman filter has better numerical properties than alternative square-root formulations, is described in Algorithm 1. The process- and measurement-noise covariance matrices are also represented using their upper-triangular Cholesky factorizations throughout the filter (Γ_W, Γ_V). The nonlinear dynamics (f) are linearized and evaluated at the corrected mean to create a prediction step, and we assume there are no control inputs from the spacecraft. We show simulation results using the SREKF in Section 6.

Algorithm 1 QR Extended Kalman Filter

```

1: function QR EKF( $\mu_{t|t}, F_{t|t}, y_{t+1}, C, \Gamma_W, \Gamma_V$ )
2:    $\triangleright$  State Prediction
3:    $\mu_{t+1|t} = f(\mu_{t|t})$ 
4:    $\triangleright$  Linearize
5:    $A = \frac{\partial f}{\partial x}|_{\mu_{t+1|t}}$ 
6:    $\triangleright$  Covariance Prediction
7:    $F_{t+1|t} = qr(F_{t|t}A^T, \Gamma_W)$ 
8:    $\triangleright$  Measurement Innovation
9:    $z = y_{t+1} - C\mu_{t+1|t}$ 
10:   $\triangleright$  Innovation Covariance
11:   $G = qr(F_{t+1|t}C^T, \Gamma_V)$ 
12:   $\triangleright$  Kalman Gain
13:   $L = [G^{-T}C]F_{t+1|t}^T F_{t+1|t}$ 
14:   $\triangleright$  State Update
15:   $\mu_{t+1|t+1} = \mu_{t+1|t} + Lz$ 
16:   $\triangleright$  Covariance Update
17:   $F_{t+1|t+1} = qr(F_t + 1|t(I - LC)^T, \Gamma_V L^T)$ 
18: end function
```

Tag State Covariance

We calculate the tag state covariance using two methods: a Monte-Carlo method with 1000 samples, and a linearized error propagation using the measurement Jacobian.

The Monte-Carlo method computes each sample by adding noise to the satellite positions and measurements to simulate the satellite state uncertainties and measurement errors. The noise on the satellite position was sampled from a Gaussian with the covariance obtained from the SREKF. We generate a set of ground truth measurements with (1) and (3) and use a root-finding method to compute tag positions from the noisy measurements. We use Newton's method along with an Armijo line search detailed in Algorithm 2. The parameters φ, b, α in Algorithm 2 are tuned to ensure the algorithm decreases the residual at every step. Finally, we compute the mean (μ) and covariance (Σ) of the tag positions and compare them to ground truth. The metric we use to determine the position tracking accuracy is the root mean squared (RMS) error:

$$RMS = \sqrt{Tr(\Sigma_{3 \times 3})}. \quad (14)$$

Algorithm 2 Newton's Method with Armijo Line Search

```

1:  $z_t = h(x_t)$   $\triangleright$  Generate truth measurements
2: function NEWTON( $x_0$ )
3:   while  $\|r\| \geq tol$  do
4:      $r = f(x_0) - z_t$   $\triangleright$  Compute Residual
5:      $J = \frac{\partial r}{\partial x}|_{x_0}$   $\triangleright$  Residual Jacobian
6:      $\Delta x = J \setminus r$ 
7:     while  $\|r(x_0 + \Delta x)\| > \|r(x_0 + b\alpha J\Delta x)\|$  do
8:        $\alpha = \varphi\alpha$   $\triangleright$  Armijo Line Search
9:     end while
10:     $x_0 + = \alpha\Delta x$   $\triangleright$  Apply Step
11:   end while
12: end function
```

In the linearized error-propagation method, we linearize the nonlinear measurement-residual function using a first-order Taylor expansion use the resulting Jacobian matrix A to map the covariance of the satellite state and measurements into the

covariance on the tag position:

$$P_{tag} = AP_{sat}A^T \quad (15)$$

The Jacobian A is obtained using the implicit function theorem and a derivation is provided in the Appendix.

5. SOFTWARE-MODELING TOOL

We have developed an interactive software-modeling tool to visualize the effects of satellite constellation geometry on tag-position error. This tool allows the user to change orbital parameters, including altitude, right ascension of the ascending node (RAAN), and true anomaly separation between the satellites. The user can also vary the tag latitude to observe tag-position error at different latitudes. Measurement noise (timing and frequency accuracy) can also be adjusted based on the hardware specifications of the sensors onboard the satellite. The tool outputs a two-sigma covariance ellipse in the tag's local north-east-up coordinate system for both TOA and Doppler architectures. Fig. 25 in the Appendix shows the layout of the tool, which is open source and available at the following link: <https://github.com/vegaf1/SatelliteNavigation.jl>

6. RESULTS

SREKF Results

The results of the satellite trajectory estimate over five orbits are shown in Figs. 3, 4, 5. These plots only consider the x-component of position, velocity, and acceleration, while all components are shown in the Appendix. All errors are bounded by the three-sigma envelope from the filter's covariance estimate, which indicates that the filter is consistent. The RMS error of the satellite position was 1.237 m, which is nearly an order-of-magnitude improvement upon the raw GPS measurements.

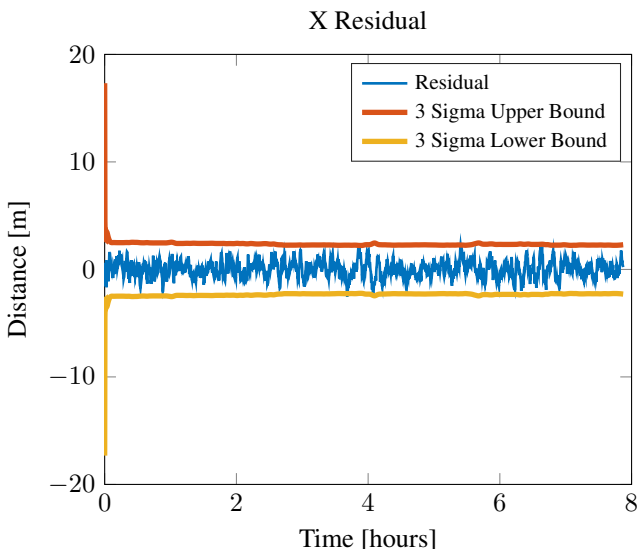


Figure 3. Orbital position errors (x-component) from SREKF estimator with DMC.

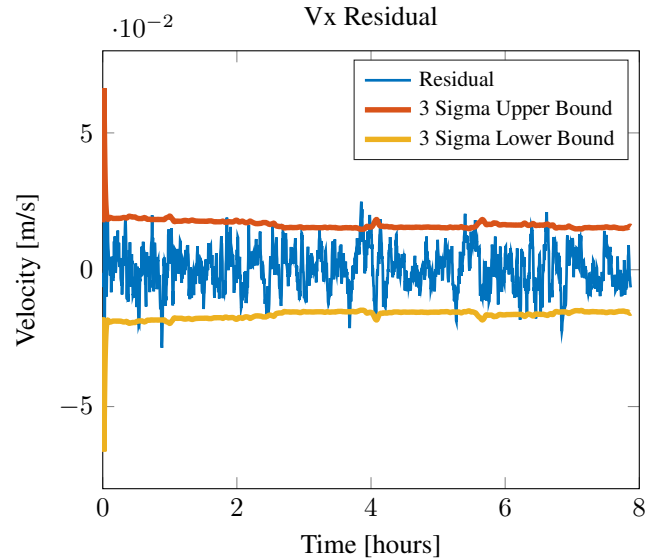


Figure 4. Estimator with DMC via first-order Gauss-Markov model and different order gravity models X velocity residual

Architecture Trade Study Results

We determine a base satellite configuration to evaluate the performance of all the architectures in Table 1. The measurement accuracy was set to be the same among all the architectures. Fig. 6 depicts the standard variables a user can change to modify the satellite geometry, and the orbit altitude can also be modified depending on the mission requirements. The satellites are placed on polar orbits, and the tag is located near the equator with the longitude in between the polar orbits. The configuration for the set of results in Figs. 7 and 8 is an altitude of 500 km, a 2 degree separation in right ascension of the ascending node, a 10 degree true anomaly separation (θ_{sep}), and a 3 degree true anomaly separation between the first satellites placed in each orbit ($\Delta\theta_{sep}$). For the architectures with one frequency, 400 MHz was used, and the dual-frequency architectures used 400 MHz and 600 MHz. The RMS tag-position error was calculated at discrete time steps along the orbit in which all the satellites are in the 70° horizon of the tag as shown in Fig. 2. This accuracy was computed using the Monte Carlo method described in Section 4. Once the satellites are out of the horizon of the tag, the algorithm returns the minimum RMS tag-position error among all the time steps in the horizon. The RMS tag-position error and bias are shown for all the architectures in Fig. 7 and Fig. 8 (the architectures are referenced by the labels in Table 1). Overall, the four-satellite dual-frequency case resulted in the best performance, with an RMS tag-position error of 60.83 meters and a bias of 1.89 meters.

The TOA method is consistently superior to the Doppler method, which we attribute to the relative sensitivity of the Doppler method to frequency measurement errors, as well as the effect of the ionosphere, which induces a frequency error of around 10 Hz, as shown in (5). Using two frequencies reduces the position bias in both methods.

The satellite configuration geometry also dramatically affects tracking performance. An analysis of these effects was performed by modifying one of orbital variable (e.g. RAAN

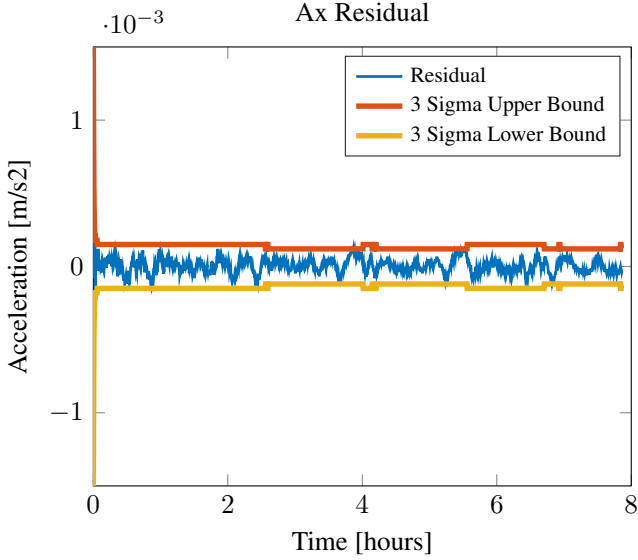


Figure 5. Estimator with DMC via first-order Gauss-Markov model and different order gravity models X acceleration residual

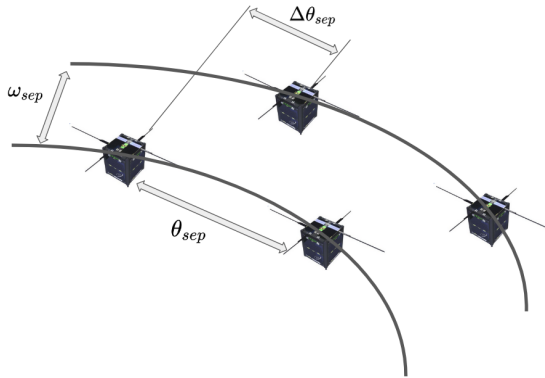


Figure 6. Satellite constellation in LEO for tracking

separation) by small increments while keeping the rest of the geometry variables constant. These tests were performed on the four-satellite TOA with two frequency architecture and the results are shown in Figs. 9-11. This analysis shows that a near-optimal configuration that minimizes tag-position error consists of a RAAN separation of approximately three degrees, a true anomaly separation of roughly eight degrees, and a delta-true-anomaly separation as large as possible. Increasing the delta true anomaly reduces the amount of time all satellites are in view of the tag simultaneously. Therefore a careful trade-off must be made.

For dual-frequency architectures, the separation between the frequencies also affects the tag-position error. Fig. 12 shows this effect; the greater the frequency separation, the lower the tag-position error. However, large separations in frequency are infeasible due to hardware and regulatory constraints.

The major source of uncertainty for all architectures is measurement noise. An analysis of these effects on the tag-position error is shown in Fig. 13-14. The tag transmit time

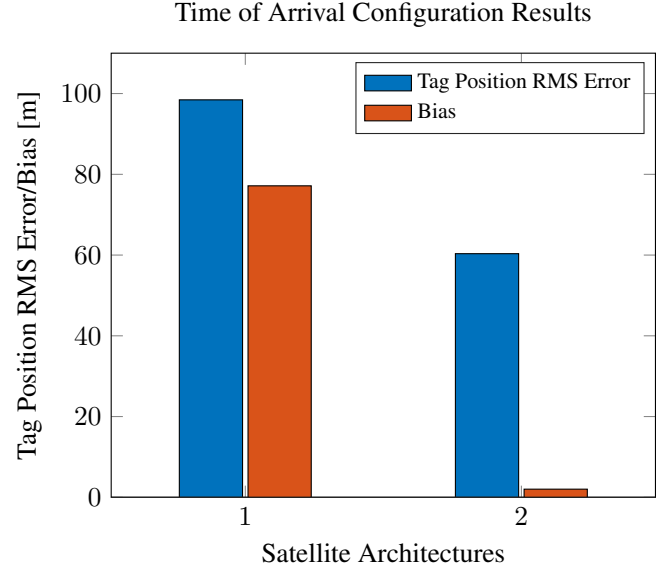


Figure 7. RMS tag-position error and bias for TOA-based satellite configurations

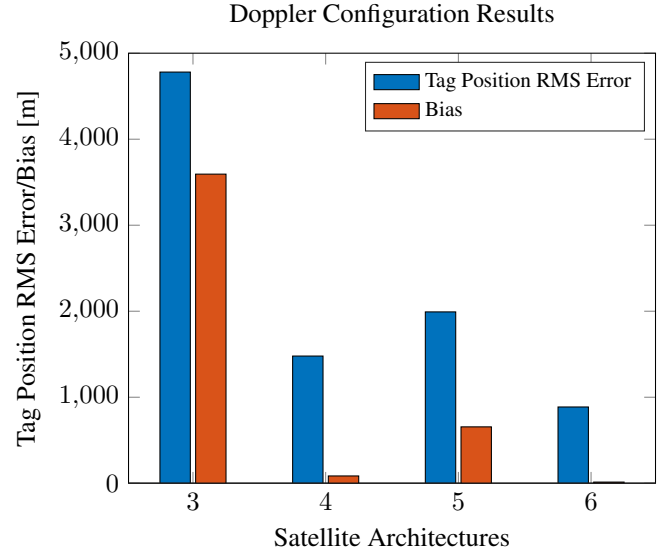


Figure 8. RMS tag-position error and bias for Doppler-based satellite configurations

is inversely proportional to the uncertainty in the frequency measurement for Fig. 14.

7. EXPERIMENTAL VALIDATION

As a proof-of-concept validation for the recommended TOA method, field testing was completed in Boulder, CO, as illustrated in Fig. 1. In the experiment, a simpler single-frequency architecture was used with the goal of demonstrating the capabilities of the system on a smaller scale. In this section, we discuss the data processing and analysis methods used in the experiment, as well as their applicability and relevance to the full system.

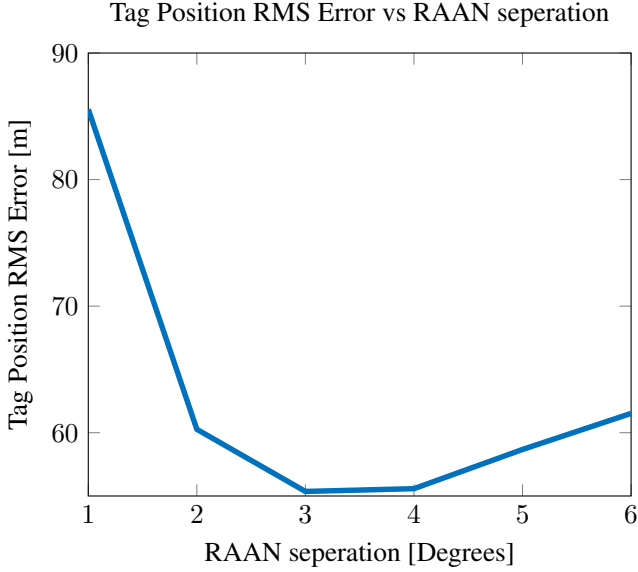


Figure 9. RMS tag-position error as the RAAN separation between orbits (ω_{sep}) increases

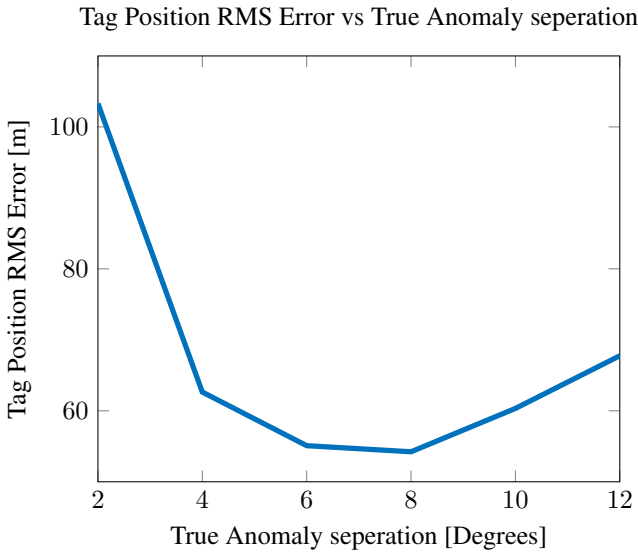


Figure 10. RMS tag position as the true anomaly (θ_{sep}) between the satellites placed on the same orbit increases

Experimental Design

Four receivers, named and henceforth referred to as Astro, Elroy, Jane, and Judy, were placed in a roughly trapezoidal configuration spaced 400-1000m from their nearest neighbors. All receivers were approximately co-planar, limiting location determination to two dimensions, instead of full positioning including altitude. In the center of the receiver constellation sat a broadcasting beacon with a known location, which was used to perform receiver clock synchronization. During testing, a simulated animal tag was moved around the field site for approximately one hour. The beacon emitted signals at a frequency of 0.1 Hz, while the tag transmitted at 1 Hz, and the receivers collected data with a bandwidth of 2.8 MHz. This

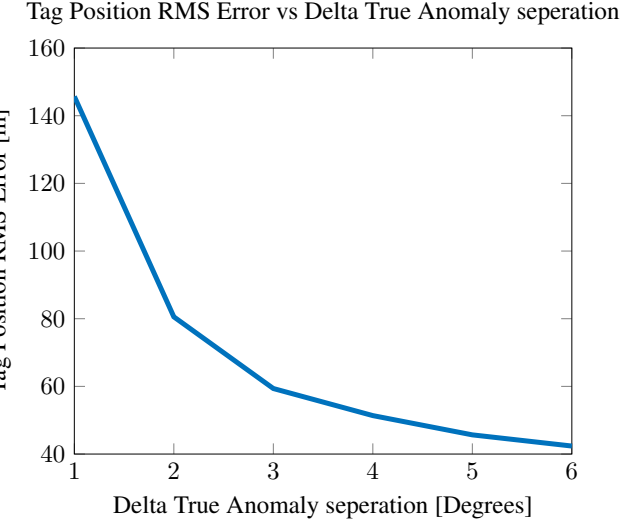


Figure 11. Tag positioning RMS error as the delta true anomaly ($\Delta\theta_{sep}$) between the first satellite of each orbit increases

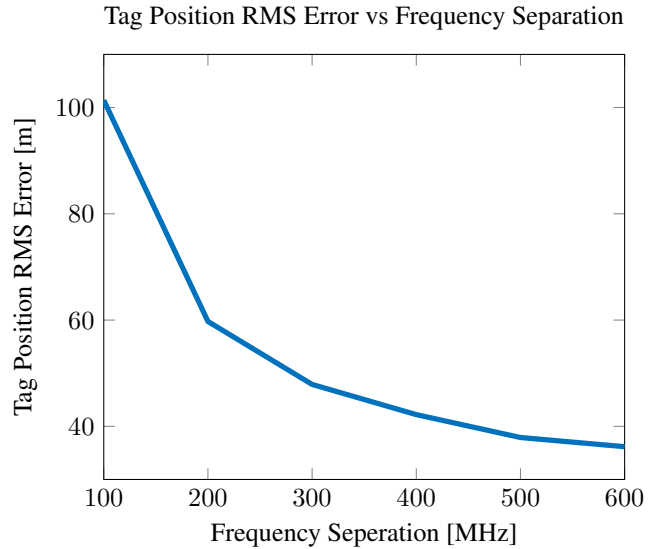


Figure 12. RMS tag-position error as the frequency separation in a dual-frequency architecture increases

yielded approximately one billion data samples per receiver over the testing time. The animal tag also collected accurate GPS data for later use in determining location residuals. For ease of computation in this scaled-down model, a local east-north-up coordinate system was employed in collecting and comparing data.

Data Processing

Following data collection, the first step in the processing sequence was correlating the raw data collected by the receivers with the known signals broadcast by the tag and beacon. Both transmitters emitted signals encoded with pseudo-random number (PRN) Gold codes, which are widely utilized in GPS applications because of their low, bounded cross-correlation

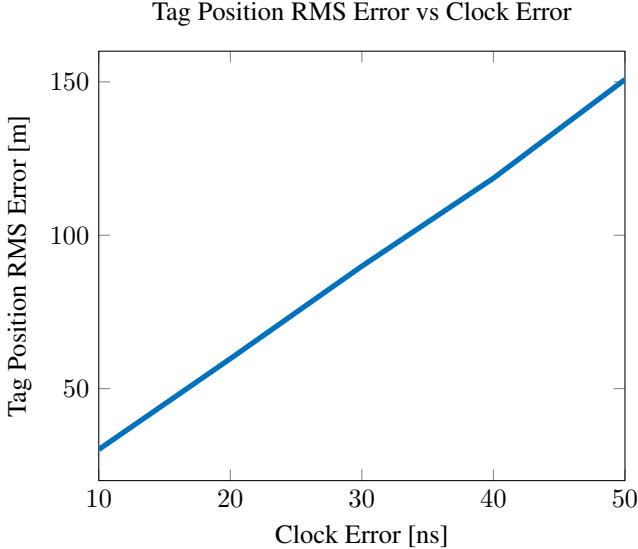


Figure 13. RMS tag-position error as the clock error increases

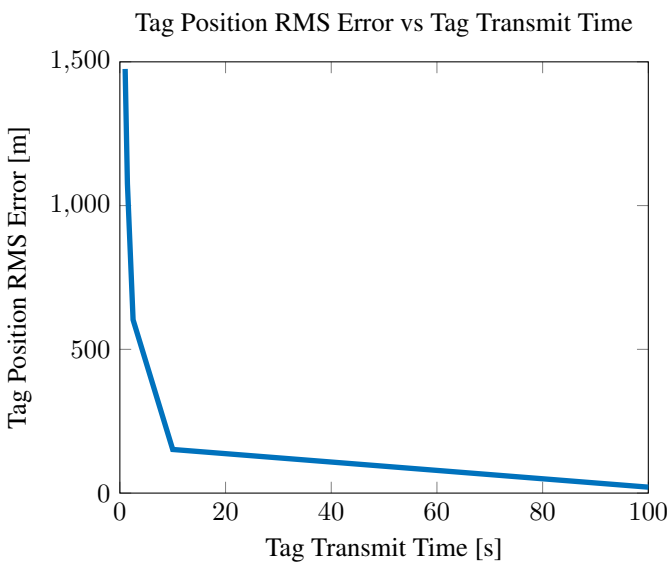


Figure 14. RMS tag-position error as the tag transmit time increases. This was tested on the dual-frequency Doppler architecture.

between unique instances [2]. This makes it possible to broadcast several codes across the same frequency range with little interference. The Gold codes used in this experiment were 1023 bits in length.

Cross correlations were computed between the recorded data from all four receivers and the known tag and beacon Gold codes. Because of the pseudo-random nature of the Gold codes, this process outputs clear spikes when the two codes align (indicating that the receiver has received the transmitted signal), and noise at all other times, as illustrated in Fig. 15.

Following cross correlation, the times associated with each

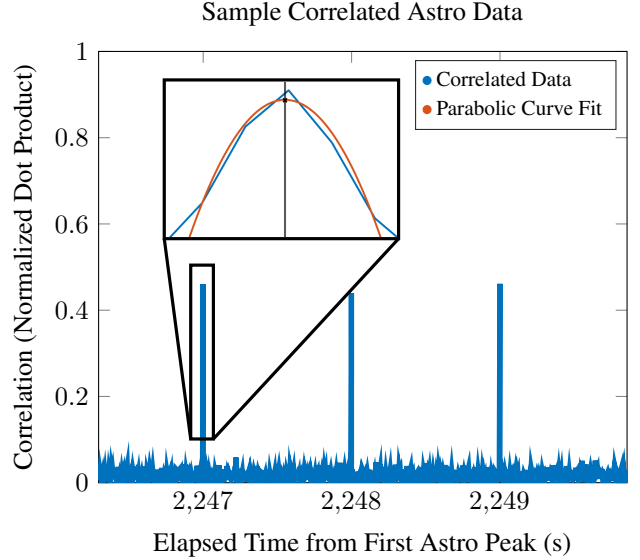


Figure 15. A sample set of peaks from the astro tag signal. Parabolic curve fitting is inset to visualize the peak determination process.

correlation peak must be computed for use in later TOA calculations. Parabolic curve fitting was used to identify peaks with sub-sample accuracy. Then, absolute time offsets between the receivers were determined using the known location of the broadcasting beacon and a simple time-of-flight calculation. Adding these offsets to the recorded tag peaks ensures that they are properly aligned to the same absolute time reference.

The final step in the data processing sequence was to calculate the locations of the tag. This process begins by identifying peaks from all receivers that correspond to the same tag pulse. Because the tag broadcasts at a predictable rate, the projected arrival times can be easily identified. However, it is expected that each receiver measures the same peak at a slightly different time. Tag positions are then calculated using the TOA method and the determined arrival times. The nonlinear least-squares problem was solved using the Levenberg-Marquardt algorithm. All signal processing was performed in MATLAB.

Predicted Outcomes

Using the parameters of the experimental setup, predicted outcomes were determined before data collection began to establish a benchmark for desired bounds on the position error. To do this, the Implicit Function Theorem was employed to determine location covariance based on a set of input variables θ , which included receiver positions, offsets, and signal arrival times. Each of these input variables was assigned an estimated variance based on unavoidable real-world measurement error in defining them; notably, 10 meters was used for each xy position, while $\sqrt{0.1}$ microseconds was used for every time evaluation. A tag position x was also established to allow for the calculation of the residual value $r(x, \theta)$.

This method produced expected variances for each of the receiver positions between 3 and 5 meters, and time errors on the order of 1×10^{-4} microseconds. Notably, variances in

the y dimension ($\mu = 4.85$) were slightly higher than those in the x dimension ($\mu = 4.05$), likely due to limitations in the experimental setup. Namely, the testing site is configured such that the receivers are placed further apart in x than they are in y, allowing for less precision in the North/South dimension than it does in the East/West direction.

Taken together, these data suggest unavoidable variance in the TOA calculations between 0.1 and 0.5 microseconds, depending on the receiver. This translates to location errors between 40 and 120 meters for each receiver independently, although the use of all four will likely reduce those values for overall location prediction. As such, data analysis was performed with an expectation of unavoidable error on the order of 10m.

Analysis

The final predicted location set is plotted alongside the actual GPS data for the tag in Fig. 18. This graph depicts a simple distance from the local origin, taking into account both x and y coordinates simultaneously. Plotted alongside these points are two additional lines depicting a 10-point moving average of the standard deviation of the set, which is approximately 22.6 meters.

Fig. 1 presents a more complete picture of position error in two dimensions, as opposed to a simple distance. In that image, it is clearer to discern where exactly predicted locations vary from actual locations, particularly in the places near the Jane and Judy receivers. In fact, there is a small section of path just to the left of the Judy receiver for which there are no location predictions, which represents one of the noisiest sections of data where clean tag peak sets could not be discerned. Similarly, location predictions vary greatly from the actual path just above the Jane receiver, which could be due to a similar noise problem.

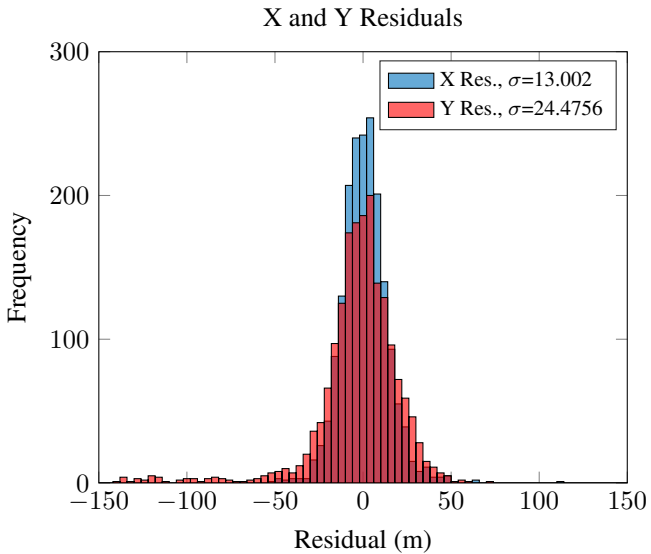


Figure 16. Histogram demonstrating the difference in residual distributions in the local x (East/West) and y (North/South) directions.

In terms of actual location residuals, Fig. 16 and Fig. 17 provide histograms of the residuals in the x and y dimensions independently, as well as the total residual values congruent

with Fig. 18. Beginning with Fig. 16, it is clear to see that the residual distributions follow an expected normal pattern. This also corroborates the result from Fig. 18, where at least 95% of the data appear to fall within the 2-standard-deviation bounds.

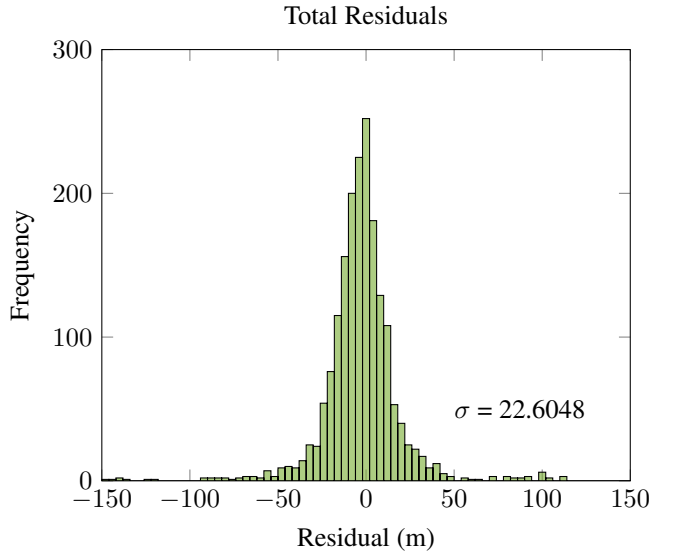


Figure 17. Histogram of total residuals.

Fig. 16 also demonstrates that there is far less error in the x direction ($\sigma = 13.002m$) than there is in the y direction ($\sigma = 24.476m$). This can likely be attributed to a few factors, beginning with the same noise issue identified in Fig. 1. Particularly, the set of outliers on the left end of the histogram clearly maps to the errors above the Jane receiver. This result also reflects the limitations of the experimental setup as predicted by the covariance analysis.

Finally, Fig. 17 provides a total residual histogram, again illustrating the expected normal distribution. The overall standard deviation for the set, $\sigma = 22.605m$ is well within an acceptable range for the goals of the experiment, particularly considering the square kilometer of the testing area. Returning to the earlier analysis of predicted variances, it is also clear to see that the results here reasonably match with the magnitude of error that was expected. This indicates that our methods of data processing and analysis are accurate and work well, as only nominal new error was introduced. Looking forward, this experiment therefore validates the proposed design, at least within its limited scope that does not include ionospheric interference.

8. CONCLUSIONS

We have presented an end-to-end simulation of a space-based wildlife-tracking system, a constellation-design trade study, a unified open-source package to test user-defined satellite geometries using both architectures, and outdoor hardware validation experiments. The four-satellite dual-frequency TOA architecture is recommended due to its superior performance and relatively low system complexity. This method of tracking provides better accuracy than ARGOS, and is more cost effective, as the proposed satellites for this mission are nanosatellites and the transmitting tags are lightweight, low-power, and low-cost. We also present preliminary results for

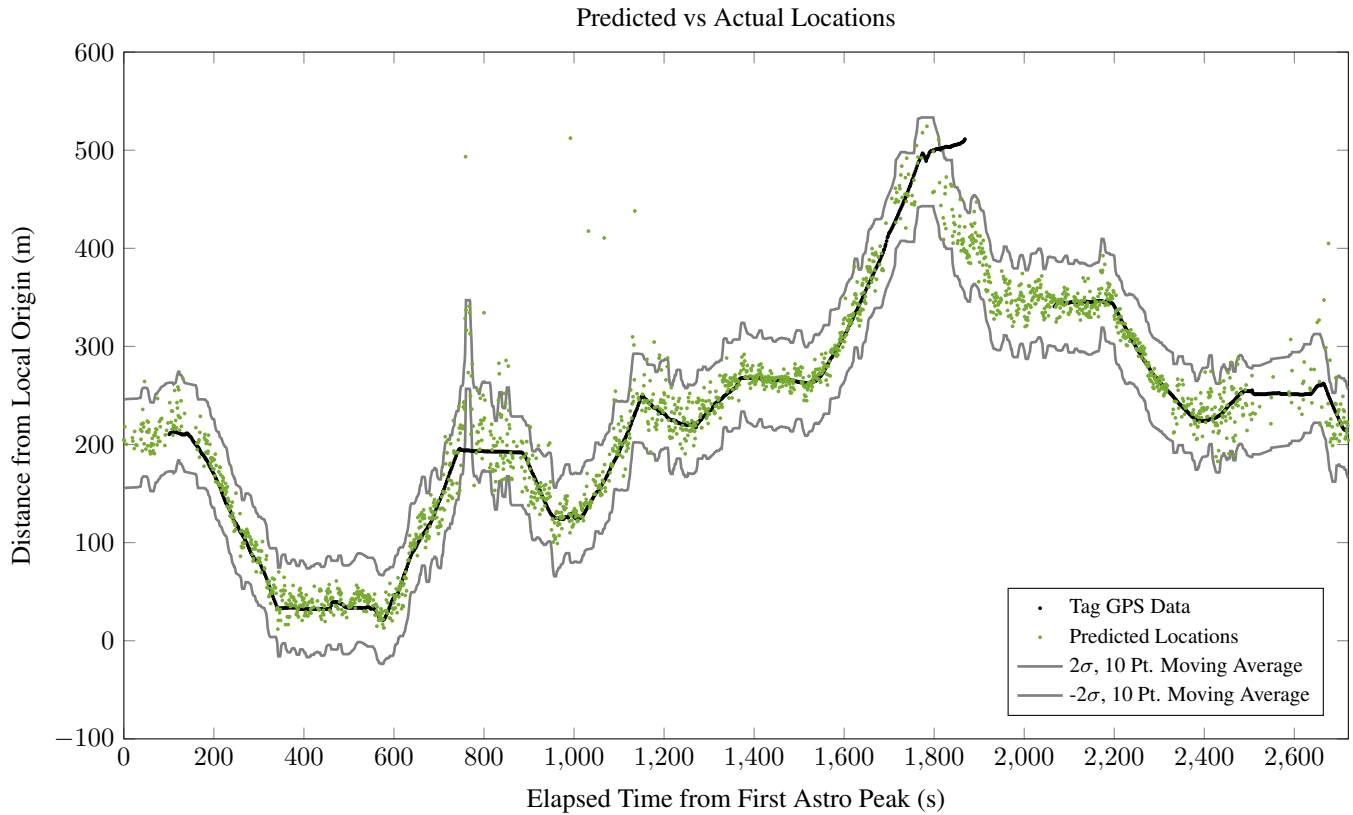


Figure 18. Scatter plot of real and predicted tag locations (distance from the local origin) over time.

hardware validation of flight-traceable receivers and tags in outdoor field tests that demonstrate the capabilities of the system on a smaller Earth-bound scale.

Future work includes implementing a batch least-squares solution to the satellite state estimation problem, which may improve state estimates. Exploring architectures with more than four satellites is another possibility to explore, as this may further reduce errors and enable estimation of more bias terms. Finally, we will seed space-based validation experiments of our TOA method on future small-satellite missions.

ACKNOWLEDGMENTS

This work was supported by the Bureau of Ocean Energy Management Environmental Studies Program under Interagency Agreement M21PG00004 and NASA under agreement 80NSSC21K0446, and in-part by a National Geographic Society Explorer's grant (NGS-54261T-18) to R. MacCurdy. F. Vega was also supported by the GEM Fellowship.

REFERENCES

- [1] R. J. Danchik, "An Overview of Transit Development," *JOHNS HOPKINS APL TECHNICAL DIGEST*, vol. 19, no. 1, 1998.
- [2] Pratap Misra and Per Enge, *Global Positioning System: Signals, Measurements and Performance*, second edition ed. Ganga-Jamuna Press, 2006.
- [3] R. B. MacCurdy, R. M. Gabrielson, and K. A. Cor-topassi, "AUTOMATED WILDLIFE RADIO TRACKING."
- [4] J. Wall, G. Wittemyer, B. Klinkenberg, and I. Douglas-Hamilton, "Novel opportunities for wildlife conservation and research with real-time monitoring," *Ecological Applications*, vol. 24, no. 4, pp. 593–601, 2014.
- [5] G. C. Hays, H. Bailey, S. J. Bograd, W. D. Bowen, C. Campagna, R. H. Carmichael, P. Casale, A. Chiara-dia, D. P. Costa, E. Cuevas *et al.*, "Translating marine animal tracking data into conservation policy and management," *Trends in ecology & evolution*, vol. 34, no. 5, pp. 459–473, 2019.
- [6] "Argos User's Manual," Jun. 2016.
- [7] M. Witt, S. Åkesson, A. Broderick, M. Coyne, J. Ellick, A. Formia, G. Hays, P. Luschi, S. Stroud, and B. Godley, "Assessing accuracy and utility of satellite-tracking data using Argos-linked Fastloc-GPS," *Animal Behaviour*, vol. 80, no. 3, pp. 571–581, Sep. 2010. [Online]. Available: <https://linkinghub.elsevier.com/retrieve/pii/S0003347210002113>
- [8] E. F. Hartel, W. Noke Durden, and G. O'Corry-Crowe, "Testing satellite telemetry within narrow ecosystems: nocturnal movements and habitat use of bottlenose dolphins within a convoluted estuarine system," *Animal Biotelemetry*, vol. 8, no. 1, p. 13, Dec. 2020. [Online]. Available: <https://animalbiotelemetry.biomedcentral.com/articles/10.1186/s40317-020-00200-4>
- [9] "Lotek PinPoint GPS Argos Solar."

- [10] M. Krondorf, S. Bittner, D. Plettemeier, A. Knopp, and M. Wikelski, “Icarus—very low power satellite-based iot,” *Sensors*, vol. 22, no. 17, p. 6329, 2022.
- [11] R. MacCurdy, R. Gabrielson, E. Spaulding, A. Purgue, K. Cortopassi, and K. Fristrup, “Automatic Animal Tracking Using Matched Filters and Time Difference of Arrival,” *Journal of Communications*, vol. 4, no. 7, pp. 487–495, Aug. 2009. [Online]. Available: <http://ojs.academypublisher.com/index.php/jcm/article/view/24>
- [12] Duncan Eddy, “SatelliteDynamics.jl.” [Online]. Available: <https://github.com/sisl/SatelliteDynamics.jl/blob/master/docs/src/index.md>
- [13] Oliver Montenbruck and Eberhard Gill, *Satellite Orbits*. Springer, 2012.
- [14] B. D. Tapley and B. E. Schutz, “Estimation of unmodeled forces on a lunar satellite,” *Celestial Mechanics*, vol. 12, no. 4, pp. 409–424, Dec. 1975. [Online]. Available: <http://link.springer.com/10.1007/BF01595388>
- [15] K. A. Myers and B. D. Tapley, “Dynamical Model Compensation for Near-Earth Satellite Orbit Determination,” *AIAA Journal*, vol. 13, no. 3, pp. 343–349, Mar. 1975. [Online]. Available: <https://arc.aiaa.org/doi/10.2514/3.49702>
- [16] J. R. Carpenter and C. N. D’Souza, “Navigation Filter Best Practices.”
- [17] Kenneth Alan Myers, “Filtering Theory Methods and Applications to the Orbit Determination Problem for near-Earth Satellites,” Ph.D. dissertation, The University of Texas at Austin, 1974.
- [18] K. Tracy, “A Square-Root Kalman Filter Using Only QR Decompositions,” Aug. 2022, arXiv:2208.06452 [cs, eess]. [Online]. Available: <http://arxiv.org/abs/2208.06452>

APPENDICES

A. IMPLICIT FUNCTION THEOREM

The Implicit Function theorem was used to find the Jacobian that relates the satellite positions and the tag positions. The derivation is shown below.

$$\begin{aligned}
 x &= [x_{tag} \quad y_{tag} \quad z_{tag} \quad b] \\
 y &= [x_{sat} \quad y_{sat} \quad z_{sat} \quad f] \\
 f(x, y) &= \frac{\partial f}{\partial x} \Delta x + \frac{\partial f}{\partial y} \Delta y \\
 \Delta x &= -(\frac{\partial f}{\partial x})^{-1} \frac{\partial f}{\partial y} \Delta y \\
 A &= -(\frac{\partial f}{\partial x})^{-1} \frac{\partial f}{\partial y} \\
 P_{tag} &= AP_{sat}A^T
 \end{aligned}$$

B. DOPPLER DERIVATIONS

The Doppler measurement model is dependent on the time derivative of the pseudo range and the derivation for this term

is shown below.

$$\begin{aligned}
 r &= \sqrt{(r_{tag} - Ar_{sat})^T(r_{tag} - Ar_{sat})} \\
 r &= ((r_{tag}^T - r_{sat}^T A^T)(r_{tag} - Ar_{sat}))^{\frac{1}{2}} \\
 r &= (r_{tag}^T r_{tag} - r_{tag}^T Ar_{sat} - r_{sat}^T A^T r_{tag} + r_{sat}^T A^T Ar_{sat})^{\frac{1}{2}} \\
 r &= (r_{tag}^T r_{tag} - 2r_{tag}^T Ar_{sat} + r_{sat}^T r_{sat})^{\frac{1}{2}} \\
 \dot{r} &= \frac{1}{2||r_{tag} - Ar_{sat}||}(r_{tag}^T \dot{r}_{tag} + \dot{r}_{tag}^T r_{tag} - 2(\dot{r}_{tag}^T Ar_{sat} \\
 &\quad + r_{tag}^T \dot{Ar}_{sat} + r_{tag}^T A \dot{r}_{sat}) + r_{sat}^T \dot{r}_{sat} + \dot{r}_{sat}^T r_{sat}) \\
 \dot{r} &= \frac{1}{2||r_{tag} - Ar_{sat}||}(r_{tag}^T \dot{r}_{tag} + \dot{r}_{tag}^T r_{tag} - 2\dot{r}_{tag}^T Ar_{sat} \\
 &\quad - 2r_{tag}^T \dot{Ar}_{sat} - 2r_{tag}^T A \dot{r}_{sat} + r_{sat}^T \dot{r}_{sat} + \dot{r}_{sat}^T r_{sat}) \\
 \dot{r} &= \frac{1}{2||r_{tag} - Ar_{sat}||}(r_{tag}^T v_{tag} + v_{tag}^T r_{tag} - 2v_{tag}^T Ar_{sat} \\
 &\quad - 2r_{tag}^T \dot{Ar}_{sat} - 2r_{tag}^T A v_{sat} + r_{sat}^T v_{sat} + v_{sat}^T r_{sat})
 \end{aligned}$$

C. ADDITIONAL PLOTS

The additional residual plots in Figs. 19, 20, 21, 22, 23, and 24 show the consistency of the filter in y and z dimension for position, velocity, and unmodeled acceleration estimation of a low-earth orbiting satellite. Fig. 25 displays the layout of the interactive software modeling tool used to obtain the tag-position error using both TOA method and Doppler measurement models given a satellite constellation geometry and sensor accuracies.

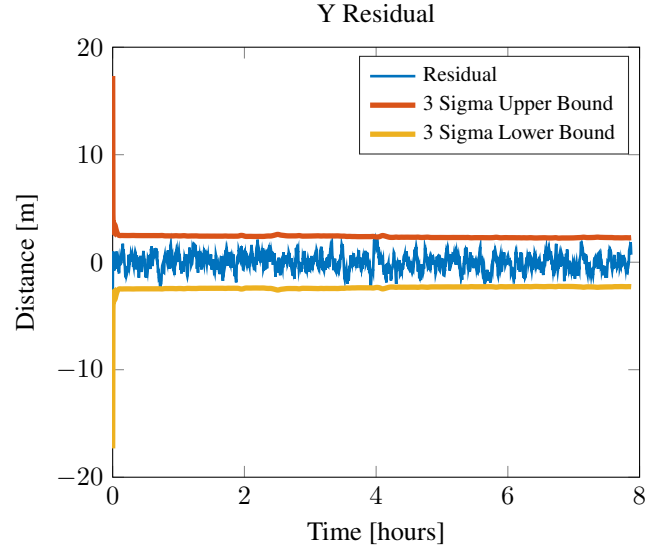


Figure 19. Estimator with DMC via first-order Gauss-Markov model and different order gravity models Y residual

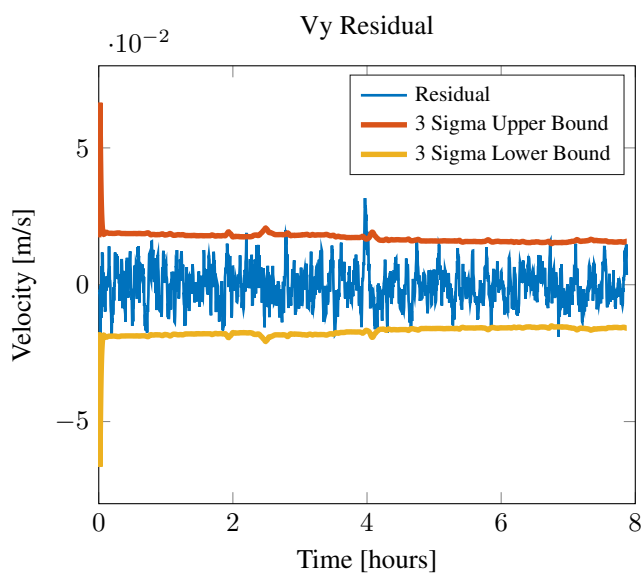


Figure 20. Estimator with DMC via first-order Gauss-Markov model and different order gravity models Y velocity residual

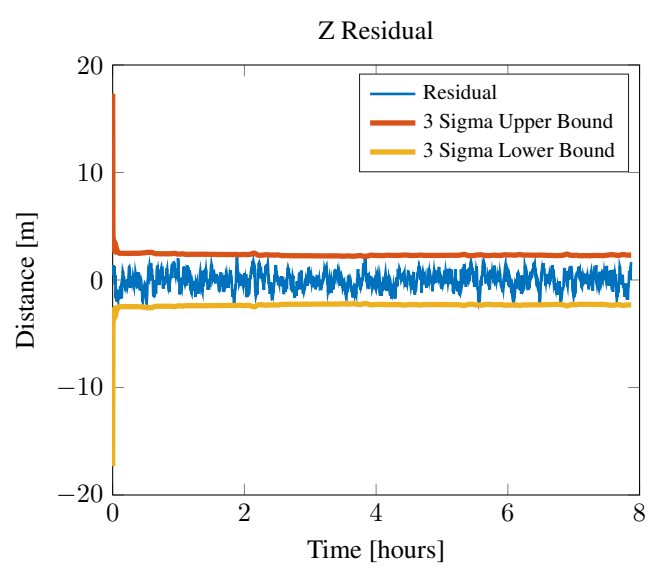


Figure 22. Estimator with DMC via first-order Gauss-Markov model and different order gravity models Z residual

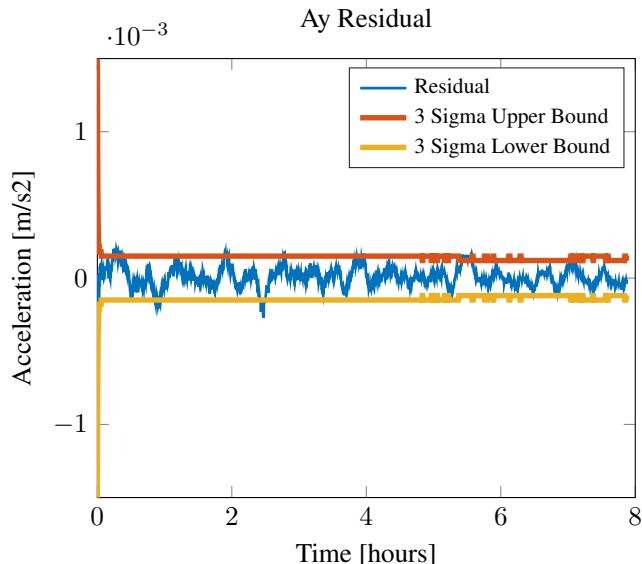


Figure 21. Estimator with DMC via first-order Gauss-Markov model and different order gravity models Y acceleration residual

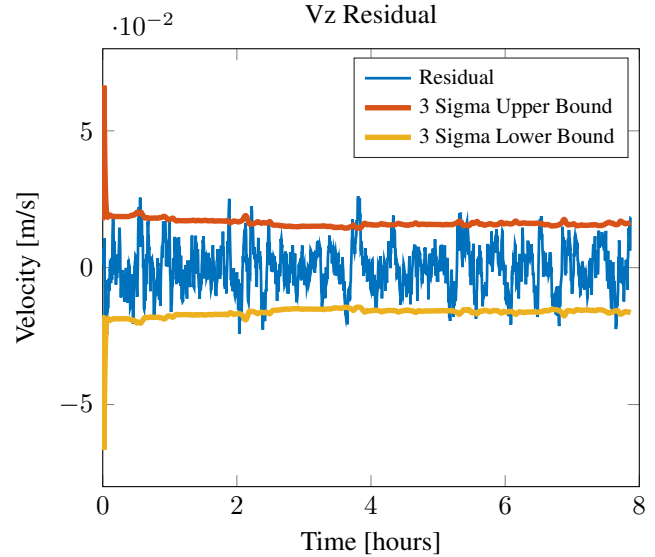


Figure 23. Estimator with DMC via first-order Gauss-Markov model and different order gravity models Z velocity residual

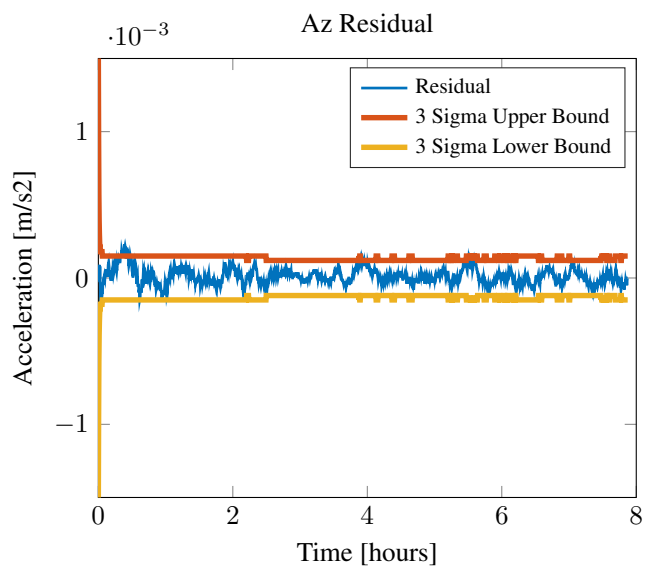


Figure 24. Estimator with DMC via first-order Gauss-Markov model and different order gravity models Z acceleration residual

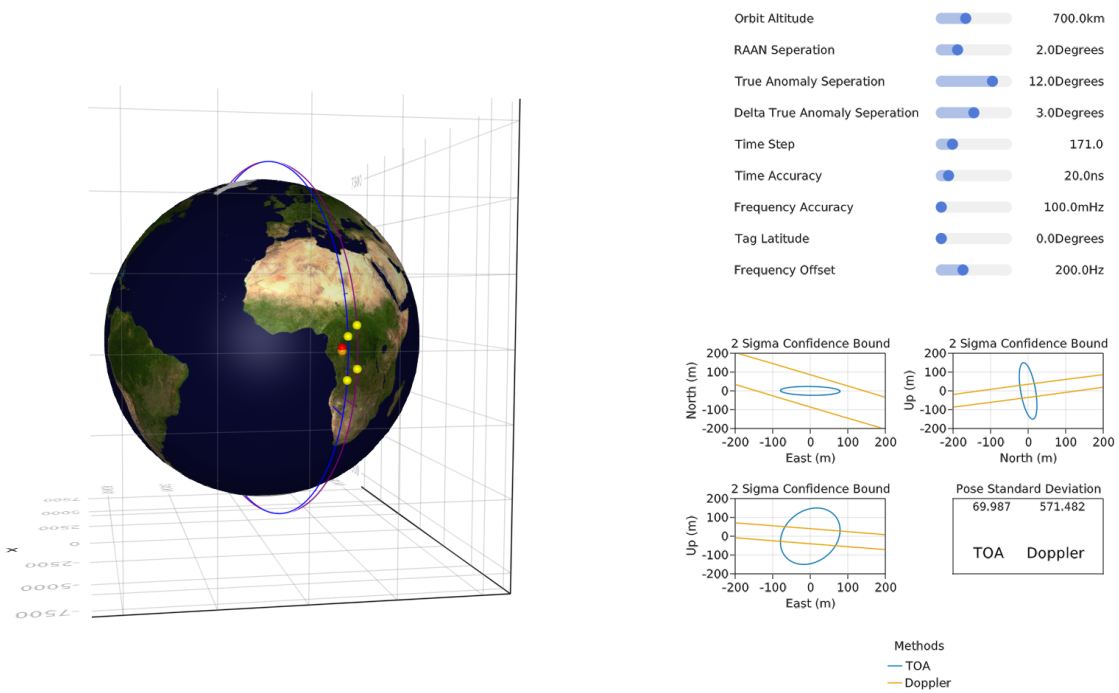


Figure 25. Interactive software modeling tool that outputs the uncertainty in the tag estimate based off the user defined satellite configuration.

BIOGRAPHY



Fausto Vega is a PhD student at the Robotics Institute at Carnegie Mellon University (CMU). He received a BS in mechanical engineering from the University of Nevada, Las Vegas and an MS in Robotics at CMU. His research interests include small spacecraft state estimation and optimal control.



James Phillips is a master's student in the school of Computer Science at the University of Colorado, Boulder. He received a BS in electrical engineering from Purdue University. His research interests include embedded systems, signal processing, and positioning, navigation, and timing.



Kathryn Lampo is an undergraduate in the School of Engineering and Applied Science at Columbia University studying mechanical engineering. She's interested in developing robotic systems for space, and her recent work has been focused on designing and engineering small satellites.



Robert MacCurdy is an Assistant Professor in Mechanical Engineering at the University of Colorado Boulder where he leads the Matter Assembly Computation Lab. He has pioneered new methods to study animal behavior in the wild, including ultra-low energy radiofrequency tracking techniques. This work originated at the Cornell Lab of Ornithology, where Rob worked as an engineer for 10 years. Rob did his PhD work with Hod Lipson at Cornell University and his postdoctoral work at MIT with Daniela Rus. He holds a B.A. in Physics from Ithaca College, a B.S. in Electrical Engineering from Cornell University, and an M.S. and PhD in Mechanical Engineering from Cornell University.



Zachary Manchester is an assistant professor in the Robotics Institute at Carnegie Mellon University and founder of the Robotic Exploration Lab. He received a PhD in aerospace engineering in 2015 and a BS in applied physics in 2009, both from Cornell University. His research interests include control and optimization with applications to aerospace and robotic systems.